nature communications

Article

https://doi.org/10.1038/s41467-025-64498-5

Robust zwitterionic hydrogels enabled by consolidated supramolecular networks and spatially hierarchical structures

Received: 10 November 2024

Accepted: 18 September 2025

Published online: 27 October 2025

Check for updates

Xingkui Guo, Lijie Zhang, Hao Zhuo, Chuyang Chen, Hang Yang, Tian Li, Haobo Qi & Wei Zhai

Zwitterionic hydrogels have emerged as promising candidates for diverse applications, especially in epidermal electronics, due to their prominent hemocompatibility, superhydration, and nonfouling properties. However, their practical applications are often severely hindered by inadequate mechanical properties and limited functionalities. Here, we develop a mechanically robust zwitterionic hydrogel with an optimal combination of functions (RHOCF) by constructing a consolidated dynamic supramolecular framework and a spatially multiscale hierarchical structure. By finely introducing a reinforced entangled supramolecular network, along with hierarchical architectures across multiple length scales into the zwitterionic hydrogel system, we can engineer highly stiff and tough zwitterionic hydrogels that seamlessly integrate typically incompatible mechanical properties, including excellent stretchability, notable tensile strength, high fracture toughness, considerable stiffness, and great resilience. The RHOCF further integrates optical transparency, ionic conductivity, self-adhesion, and freezing tolerance, enabling conformal contact with dynamic, irregular surfaces for stable motion sensing and artifact-free electrophysiological signal acquisition.

Zwitterionic hydrogels, composed of three-dimensional (3D) networks of hydrophilic polymers with intrinsically paired oppositely charged ionic groups, usually exhibit excellent hemocompatibility, antifouling, and ionic responsiveness, making them highly promising for biomedical and intelligent systems, particularly in epidermal electronics[1–4]. Nevertheless, most zwitterionic hydrogels reported to date are mechanical weakness or brittleness, despite notable advances that have substantially enhanced their mechanical performance[5,6]. A key breakthrough is the development of double-network zwitterionic hydrogels[7,8], which achieve high toughness through the incorporation of sacrificial bonds that efficiently dissipate mechanical energy[9–11]. However, these toughened zwitterionic hydrogels still suffer from the classic trade-off between strength and toughness[12]. For example, their fracture stress generally remains within the low megapascal range unless reinforced with rigid supramolecular backbones or engineered to incorporate anisotropic network structures[13,14]. This intrinsic limitation is particularly evident in structurally stable zwitterionic hydrogels supported by covalently crosslinked networks, whose tensile strength typically falls below 2 MPa[15,16].

Another major challenge in the advancement of zwitterionic hydrogels for epidermal electronics—where multifunctionality is essential—lies in combining functional versatility (e.g., self-adhesion, conductivity, and freezing resistance) with uncompromising mechanical performance[17,18]. Recent efforts to enhance toughness and strength have primarily focused on structural engineering through meticulous process modulation, including sequential crosslinking, immersion treatments, and cyclic thermal processing[19,20]. However, these approaches often undermine the integration of diverse functionalities[21]. In contrast, traditional ionically crosslinked hydrogels exploit dynamic and reversible noncovalent metal–ligand interactions to enable multifunctional properties. Yet, they generally suffer from low mechanical strength, with fracture stress typically confined to the

Department of Mechanical Engineering, National University of Singapore, Singapore, Singapore. e-mail: mpezwei@nus.edu.sg

kilopascal range[22,23]. As a result, despite their promising functionalities in epidermal electronics, these zwitterionic hydrogels fail to meet the mechanical demands required for long-term stable use[14]. Therefore, overcoming this dichotomy and simultaneously achieving both robust mechanical integrity and functional integration remains a formidable challenge in the development of zwitterionic hydrogel systems.

In biological systems, evolutionary processes have naturally endowed biomaterials (e.g., skeletal muscle and articular cartilage) with a sophisticated combination of high mechanical strength and multiple functions[24,25]. A unifying characteristic of these materials is defined by the synergistic integration of consolidated molecular frameworks and multiscale hierarchical architectures. At the molecular scale, they are composed of well-assembled protein networks (e.g., collagen fibers and actin–myosin complexes), hydrophilic biopolymers, and metal ions, which collectively form densely entangled structures exhibiting both stiffness and viscoelasticity[26,27]. At the spatial structure, these systems represent hierarchical organization spanning nanometers to macroscopic dimensions, effectively contributing to enhanced toughness and improved energy dissipation[28,29]. Inspired by these principles, various approaches (e.g., self-assembly, ice-templating, and biomineralization) have been developed to engineer robust hydrogels[30–32]. Building upon these advances, biomimetic supramolecular frameworks with multiscale structural hierarchy offer a highly promising strategy to create zwitterionic hydrogels that combine high toughness, stretchability, strength, stiffness, and multiple functions.

Here, we report an approach that involves consolidated supramolecular networks and spatially hierarchical structures to create a robust zwitterionic hydrogel with an optimal combination of functions (referred to as RHOCF). In our RHOCF (Fig. 1a), polyzwitterionic salt (PZS) and polyvinyl alcohol (PVA) were employed to form a reversible, entangled large-strain matrix. Importantly, the trivalent metal bismuth ions with high coordination ability and excellent structural stability were incorporated as the crosslinking sites to engineer spatial hierarchy and further strengthen the supramolecular network. These ions are known for their high ion mobility as well as excellent electromechanical conversion characteristics[33–35]. Furthermore, a dynamic reversible percolation behavior was established within the zwitterionic hydrogel networks, effectively enhancing its mechanical properties. Thus, the obtained RHOCF exhibited a distinctive combination of properties that are challenging to achieve simultaneously in previous studies (Fig. 1b–e). For example, the RHOCF demonstrated intrinsically high stretchability (1635%), strong tensile strength (7.93 MPa), prominent fracture toughness (76.85 MJ m^{-3}), excellent stiffness (5.27 MPa), and enhanced rebound resilience (95.65%). Strikingly, the RHOCF also displayed a high ionic conductivity (5.61 S m^{-1}), great optical transparency (>96.32% in visible light), good anti-freezing resistance (−71.61 °C), and excellent adhesion (21.9 kPa on steel). Given these merits, smart epidermal electronics were configured using our RHOCF, demonstrating superbly stable and reliable multimodal sensing performance. Concisely, this work elucidated the broad potential of the RHOCF, as a single homogeneous material platform, opening up a promising horizon to fabricate a versatile system for more integrated intelligent epidermal electronics.

Results

Design of the RHOCF

As illustrated in Fig. 1a, we developed a robust zwitterionic hydrogel with an optimal combination of functions (RHOCF) by integrating consolidated supramolecular networks and spatially hierarchical architectures. The system was strategically engineered using poly([2-(methacryloyloxy) ethyl] dimethyl-(3-sulfopropyl) ammonium hydroxide–acrylic acid) (PZS) chains, polyvinyl alcohol (PVA) chains, and bismuth ions (Supplementary Fig. 1). PZS chains possess intrinsic

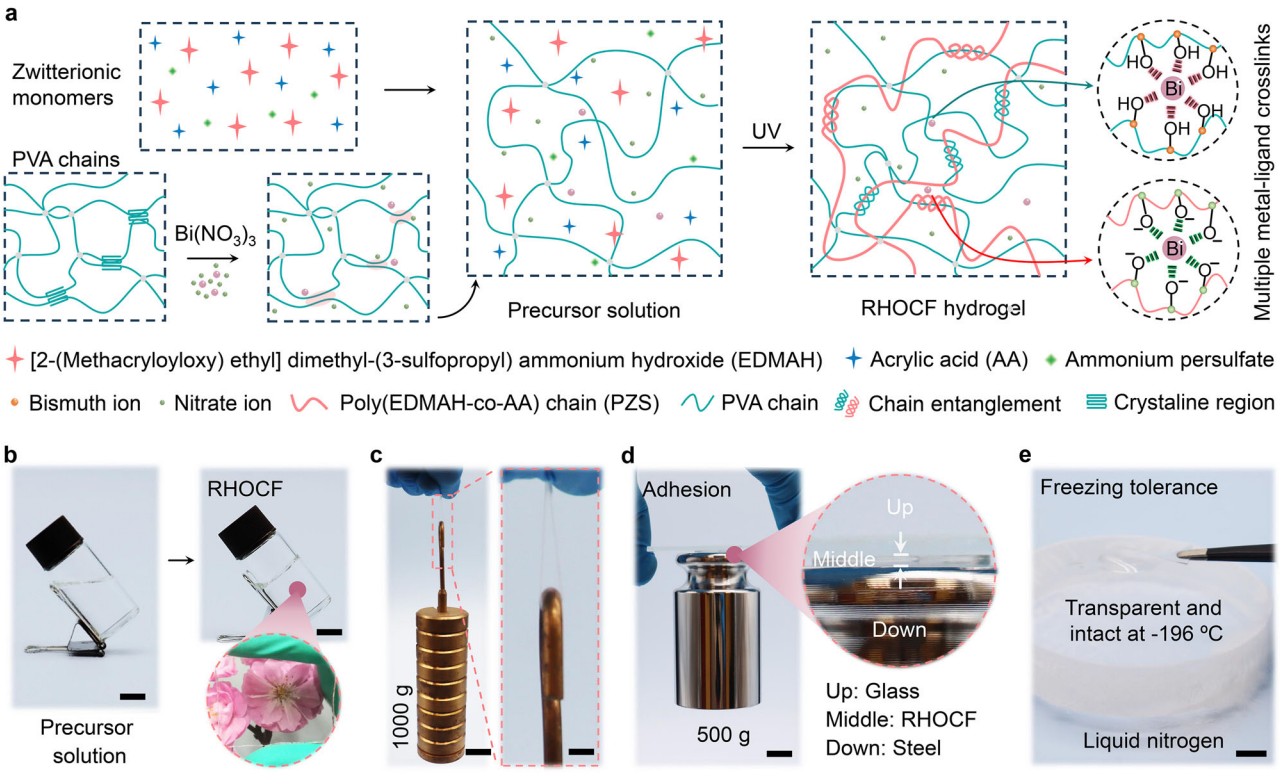

Fig. 1 | Schematic of the RHOCF. a Schematic illustration of architectures of the RHOCF. **b** Photos of the precursor solution and the transparent RHOCF. Scale bar: 1 cm. **c** Optical images of the RHOCF lifting a 1000 g weight. Scale bar: 2 cm (left) and 0.3 cm (right). **d** Images showing the lifting of a 500 g weight via the RHOCF adhesive. Scale bar: 1 cm. **e** The twisted RHOCF was placed into liquid nitrogen and still maintained its transparent and intact at −196 °C. Additionally, the RHOCF rapidly recovered to its initial state upon returning to ambient temperature. Scale bar: 1 cm.

rigidity due to strong electrostatic interactions and limited conformational flexibility, which restrict their capacity for extensive chain entanglement. In contrast, PVA is a highly flexible, linear polymer chain, offering substantial chain mobility. This enables PVA chains to penetrate and intertwine with the stiffer PZS network, resulting in a more physically entangled and mechanically reinforced structure than achievable by PZS alone. Unfortunately, the zwitterionic nature of PZS promotes electrostatically driven self-aggregation, and PVA tends to form nanocrystalline domains via intra/intermolecular hydrogen bonding. Both effects contribute to a pronounced phase separation, ultimately impairing the mechanical strength and optical clarity of the hydrogel. Inspired by natural load–bearing tissues, we introduced metal ions to suppress self-aggregation of polymer chains, enhance homogeneity, and promote interchain entanglement for forming consolidated supramolecular networks (Supplementary Fig. 2). To identify the most suitable metal ion for hydrogel formation, a series of candidates, including Ca^{2+}, Zn^{2+}, Co^{2+}, Fe^{3+}, Eu^{3+}, Al^{3+}, and Bi^{3+}, were systematically evaluated. The results revealed that Fe^{3+} failed to yield a hydrogel film within this system, indicating poor compatibility with the polymer matrix. Co^{2+} and Al^{3+} enabled gelation but resulted in undesirable features, such as deep coloration and opacity, respectively (Supplementary Fig. 2a). In contrast, Bi^{3+} stood out, exhibiting the highest mechanical strength and optical transparency (Supplementary Fig. 2b–d). These advantages were attributed to its strong coordination ability, colorlessness, non-toxicity, and compatibility with polymer matrices—surpassing traditional ion–polymer systems[36,37]. Despite its favorable properties, trivalent bismuth salts (e.g., $Bi(NO_3)_3{\cdot}5H_2O$) are almost insoluble in pure water due to hydrolysis, which generates a white precipitate of basic bismuth nitrate ($BiONO_3$) ($Bi(NO_3)_3 + H_2O \rightarrow BiONO_3 + 2HNO_3$, Supplementary Fig. 3a). Although bismuth salts dissolve in glycerol, the high viscosity of glycerol impedes solute diffusion, rendering the process kinetically unfavorable (Supplementary Fig. 3b). As displayed in Supplementary Fig. 3c–f, with the increase of glycerol content in water, the solubility of bismuth nitrate pentahydrate was greatly improved. As a result, the binary solvent system of water and glycerol finely tuned the solvation environment, promoting efficient dissolution and homogeneous dispersion of bismuth ions within the polymer matrix, which was critical for the formation of a structurally uniform and well-coordinated network. Furthermore, the incorporation of bismuth ions reinforced the polymer matrix by forming multiple dynamic metal–ligand coordination bonds that have different crosslinking kinetics and binding energy with $-SO_3^-$ groups on PZS chains and −OH groups on PVA chains, strengthening interchain interactions and inducing localized densification and network contraction, which leads to the formation of nanoscale confinement within larger pores.

To preliminarily validate the above structural design, we systematically compared the mechanical properties of pure PZS (pure zwitterionic hydrogel), PZS/PVA (zwitterionic hydrogel with an entangled network), and RHOCF hydrogels (zwitterionic hydrogel with a consolidated supramolecular network and a spatially hierarchical structure), as shown in Fig. 2a. The pure PZS hydrogel exhibited a tensile strength of 0.10 MPa and an ultimate strain of 1379%. Upon introducing PVA into PZS hydrogel to form a physically entangled network, the obtained PZS/PVA hydrogel showed a significantly increased tensile strength of 0.57 MPa, albeit with reduced stretchability (539%). Surprisingly, further enhancement was achieved by incorporating bismuth ions at varying concentrations (0.05–0.35 wt.%), forming multiple reversible metal–ligand coordination complexes (Fig. 2b). The mechanical properties improved with increasing bismuth content, peaking at 0.25 wt.%, beyond which rigidity increased and stretchability declined. Accordingly, a bismuth content of 0.25 wt.% was selected as the optimal formulation. This hydrogel exhibited a tensile strength of 7.93 MPa—representing a 79-fold and 13.9-fold increase compared to the pure PZS and PZS/PVA hydrogels, respectively—while maintaining an ultimate strain of 1635%, indicating a well-balanced enhancement of strength and extensibility. Notably, the higher bismuth ion content resulted in more metal–ligand coordination complexes, leading to greater energy requirements to deform the polymer chains. This is reflected by the tensile modulus, with values for the samples at σ=0, 0.05, 0.15, 0.25, and 0.35 being 1.53, 2.21, 3.96, 5.27, and 5.92 MPa, respectively (Supplementary Fig. 4). These mechanical properties surpass those of many previously reported hydrogel systems, underscoring the efficacy of the cartilage-like structural strategy (Fig. 2c and Supplementary Table 1).

Furthermore, cyclic loading-unloading tensile tests were performed to evaluate the resilience, energy dissipation, and the fatigue behaviors of the RHOCF (Fig. 2d, e and Supplementary Figs. 5–7). The results indicated that the RHOCF displayed highly resilient (95.65% recovery at 100% strain), comparable to well-known highly resilient materials such as elastin in human skin and arteries (~90%), resilin in dragonfly tendons (92–97%) (Fig. 2e)[21]. Notably, it demonstrated high energy dissipation, with the dissipation ratio rising to ~60% at 700% strain, attributed to efficient stress transfer and energy absorption enabled by the reinforced chain entanglement and hierarchical architecture. Fatigue resistance was further confirmed via cyclic tensile testing on pre-notched samples, in which the RHOCF sustained 12,000 cycles without observable crack propagation (Supplementary Fig. 6a), corresponding to a high calculated fatigue threshold of ~351 J m^{-2} (Supplementary Fig. 6b). While traditional hydrogels often sacrifice stretchability for enhanced strength and stiffness, the incorporation of bismuth ions in the PZS/PVA system simultaneously improved all three mechanical attributes, highlighting the effectiveness of the material design. For comparison, the comprehensive mechanical behaviors of hydrogels reported in the previous literature are summarized in Fig. 2f[25,38–42] and Supplementary Table 1.

Synergistic strengthening and toughing mechanisms of the RHOCF

Compared to the pure PZS hydrogel, the RHOCF exhibited markedly enhanced stretchability, strength, and stiffness. As a result, its fracture toughness, quantified as the total mechanical energy absorbed, increased by approximately 107 times from 0.72 MJ/m^3 in the pure PZS hydrogel up to 76.85 MJ m^{-3} (Supplementary Fig. 4). To understand the synergistic strength and toughness enhancements, the effects of the specific molecular interactions and multiscale structures within the RHOCF hydrogel were carefully investigated. On the molecular scale, the − OH groups of PVA and the $-SO_3^-$ groups of PZS were supposed to form metal–ligand coordination with bismuth ions within the resultant hydrogels, and these were validated via Fourier transform infrared spectroscopy (FTIR) and X-ray photoelectron spectroscopy (XPS). As shown in Fig. 3a, the vibration bands around 1036.1 cm^{-1} ($-SO_3^-$ symmetrical stretching vibration) displayed a redshift in the RHOCF. Meanwhile, the vibration band at 3359.4 cm^{-1} was resolved into two distinct bands, namely 3369.5 and 3214.2 cm^{-1}, which were ascribed to the stretching vibration of free and hydrogen-bonded −OH groups within polymer networks, respectively[43]. Based on the ratio of each peak, increasing the bismuth ion concentration led to an increase in the peak ratio at 3214.2 cm^{-1}, while the peak ratio at 3369.5 cm^{-1} reduced. These results convinced us that compared with control samples, the molecular interaction within the RHOCF became stronger. Importantly, the XPS results were consistent with above results (Fig. 3b). Concomitantly, robust intermolecular interactions could result in a reversible reconfiguration of the percolated network within the supramolecular structure of the RHOCF (Supplementary Fig. 7) which could selectively reinforce their mechanical performances, as also evidenced through a uniaxial cyclic loading test (Supplementary Fig. 8). To further validate the above observed molecular interactions and elucidate their formation mechanisms, density functional theory

https://doi.org/10.1038/s41467-025-64498-5

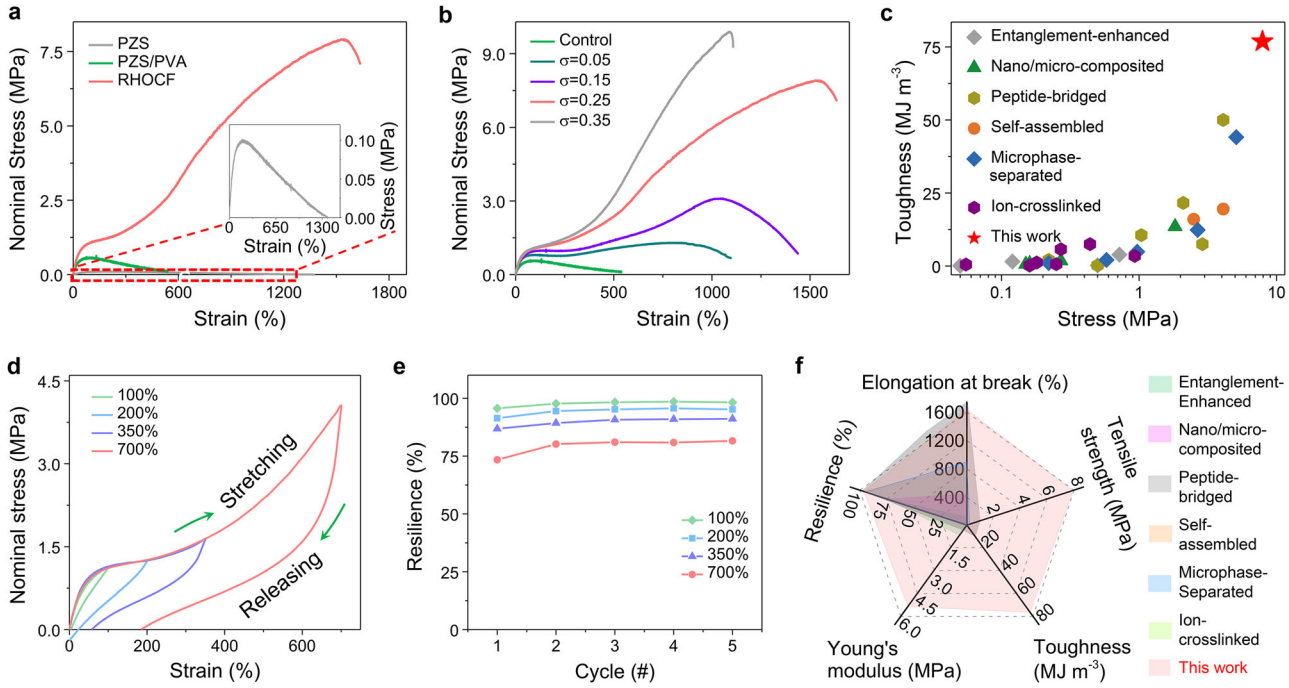

Fig. 2 | Mechanical properties of the RHOCF. a Tensile stress-strain curves of the PZS, PZS/PVA, and RHOCF samples. **b** Effect of bismuth ion contents on the tensile properties of hydrogel films. **c** Comparison of tensile strength and toughness properties between the RHOCF and other reported hydrogels reinforced by different strategies, including entanglement-enhanced, nano/micro-composited, peptide-bridged, self-assembled, microphase-separated, and ion-crosslinked. The detailed data are summarized in Supplementary Table 1. **d** Cyclic loading-unloading curves of the RHOCF. **e** Resilience of the RHOCF calculated from the corresponding cyclic loading-unloading curves. **f** Comprehensive mechanical properties of the RHOCF compared with other enhanced hydrogels reported in the literature.

(DFT) calculations were conducted to determine the binding energies of bismuth ions with PZS and PVA chains. The calculations employed the B3LYP/6-311 G(*d*, p) basis set. The optimized structures and calculated electrostatic potential (ESP) distributions of the units are shown in Fig. 3c, indicating strong metal–ligand coordination, with attractive potential concentrated on the oxygen atom of sulfonate of PZS and oxygen atom of hydroxy of PZS. On the one hand, bismuth ions could readily bond with the −OH groups of PVA chains through metal–ligand interactions. Notably, this interaction demonstrated higher binding energies (−81.3 kcal/mol) than that between the −OH groups of PVA molecules themselves, which was only −7.3 kcal/mol (Fig. 3h). This indicated that PVA was prone to form coordination bonds with bismuth ion rather than hydrogen bonding itself. On the other hand, the negatively charged oxygen atoms of PZS formed hydrogen bonds with the positively charged bismuth ions, with the binding energy between bismuth ions and PZS calculated to be −163.2 kcal/mol (Fig. 3d). Clearly, this metal–ligand coordination exhibited higher binding energies than that the electrostatic interaction between $-N^{+}(CH_3)_2-$ groups and $-SO_3^{-}$ groups (−12.9 kcal/mol). These calculations confirmed the above molecular characterizations and validated the proposed molecular interaction design within the RHOCF. Thus, the entangled polymer network was synergistically reinforced by strong ($Bi^{3+}/-SO_3^{-}$) and weak ($Bi^{3+}/-OH$) metal–ligand coordination. Importantly, the dynamic structural evolution of our strong and tough hydrogels (Supplementary Fig. 9) was investigated at the molecular level via the coarse-grained molecule dynamic (CG-MD) simulations. As shown in Supplementary Fig. 9a, the RHOCF displayed much better performance than that of the control model, qualitatively aligned with experimental results in Fig. 2a. Specifically, the polymer chain extension and sliding while stretching to 150% accounted for the ultra-elastic characteristics of the RHOCF (Supplementary Fig. 9b, c). We also noted that while stretching, the density distribution of the bismuth-based complexes at different strains showed negligible difference (Supplementary Fig. 9d). This is ascribed to the dynamic behavior of metal–ligand coordination bonds where dissociation–reformation events prevailed when stretching.

As shown in Fig. 3e, f and Supplementary Fig. 10, combining the small-angle and wide-angle X-ray scattering (SAXS/WAXS) was employed to further determine their nanoscale structures of hydrogels. As the concentration of bismuth ions increased, the intensity of peaks in both curves diminished. Especially, the diffraction peak (q=1.56 A^{-1}) in WAXS patterns weakened (Fig. 3e, f), and the peak value q_{max} from SAXS patterns shifted towards a lower q region (Supplementary Fig. 10a) with the increase of the bismuth ion concentration within the RHOCF. Based on Bragg's law $L = 2\pi/q_{max}$ which reflected the average distance between neighboring crystallites, these changes implied that a relatively larger long period was favored in the resultant hydrogels (Supplementary Fig. 10b). This is further validated by atomic force microscopy (AFM) measurements (Supplementary Figs. 11 and 12)[44–47]. The variations in SAXS and WAXS were attributed to the substantial reduction in crystallinity, wherein a large proportion of polymer chains were closely crosslinked by bismuth ions instead of forming crystals, which was beneficial for creating an enhanced crosslinking yet homogenous hydrogel network. Additionally, scanning electron microscope (SEM) images were also employed to further investigate the micro-/nano-scale structure of the RHOCF. As shown in Fig. 3g, h and Supplementary Fig. 13, the control and RHOCF samples exhibited clearly porous structures, suggesting the formation of an inerratic interpenetrating polymer network configuration between different polymer chains, rather than agglomeration. Notably, unlike the control sample, which had a typical irregular large-pore structure at the micrometer scale (Supplementary Fig. 13a), the hydrogel showed a gradual decrease in pore size and an increasingly uniform distribution with increasing bismuth ion content. Importantly, when the ratio is more than 0.15 wt.%, the hydrogels featured a well-defined hierarchical porous morphology with micrometer-scale primary pores embedded with numerous nanometer-scale pores (Fig. 3a, b). This phenomenon could be attributed to the dynamic coordination

https://doi.org/10.1038/s41467-025-64498-5

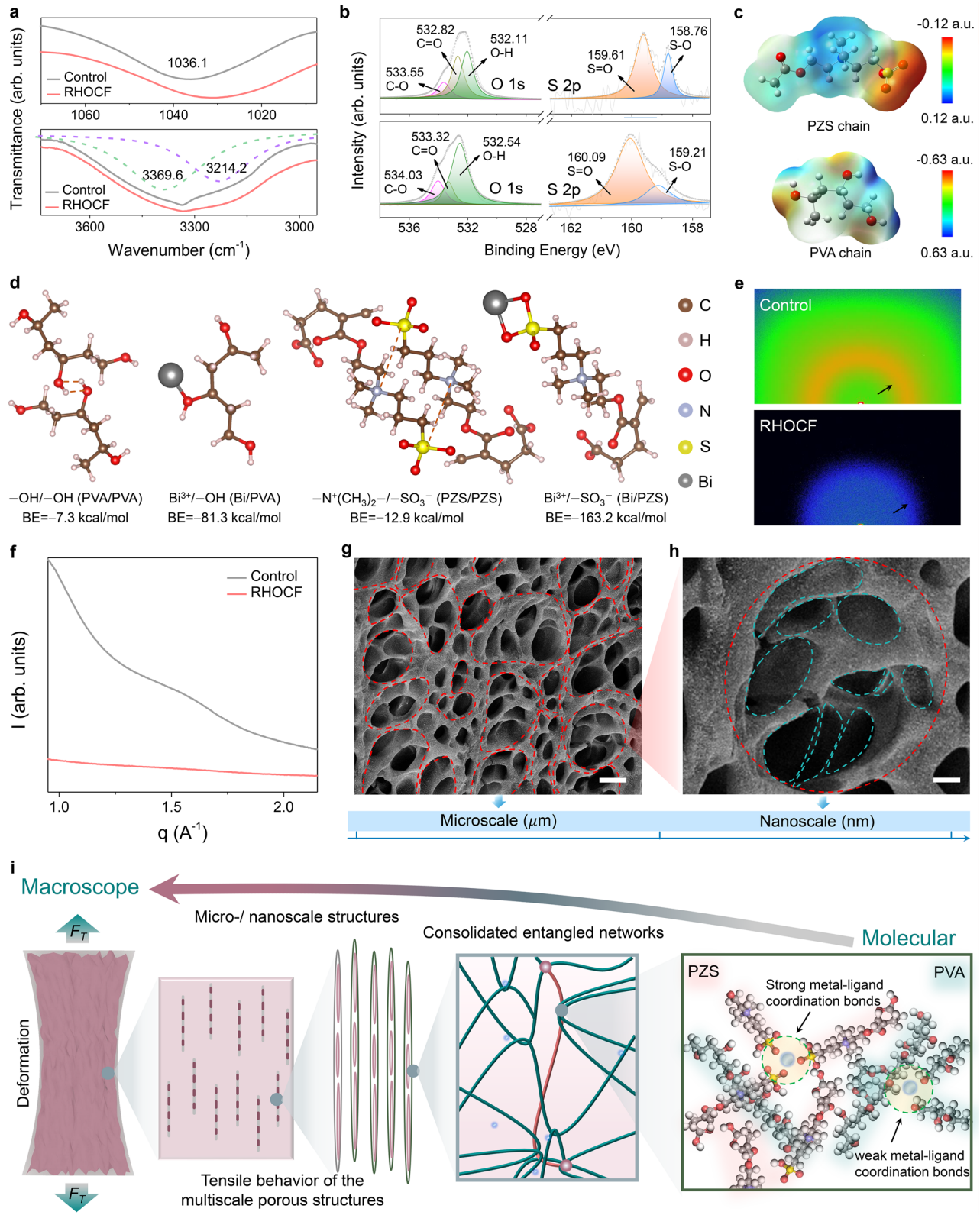

Fig. 3 | Principle for the RHOCF. a ATR-FTIR spectra of the control and RHOCF samples. **b** XPS spectra of control (up) and RHOCF (down) samples. **c** Optimized structures and electrostatic potential (ESP) distribution of PZS (up) and PVA (down) chains. **d** From DFT theoretical simulation, the binding energies of −OH/−OH, $-N^{+}(CH_3)_2-/-SO_3^{-}$, bismuth ion/−OH, and bismuth ion/$-SO_3^{-}$ are −7.3, −12.9, −81.3, and −163.2 kcal/mol, respectively. WAXS patterns (**e**) and the integrated curves (**f**) of the control and RHOCF samples. SEM images showing the microstructure (**g**) and nanostructure (**h**) of the RHOCF. Scale bars, 1 μm (**g**); 200 nm (**h**). **i** Illustration of synergistic strengthening and toughing mechanisms in the RHOCF.

crosslinking of bismuth ions within the hydrogel network and its influence on the gelation rate[48–51]. Specifically, bismuth ions, as high-charge-density metal ions, could form multiple coordination bonds with functional groups (e.g., $-SO_3^-$ and $-OH$) within the hydrogel, thereby enhancing local crosslinking density. At no or low bismuth ion concentrations, the crosslinking within the hydrogel network was relatively uniform, resulting in larger pores. As the bismuth ion concentration increased, the intensified coordination led to localized network contraction, hindering the growth of larger pores and promoting the formation of smaller ones. Nevertheless, higher bismuth ion concentrations may have accelerated the gelation process, causing uneven solidification rates in different regions of the hydrogel. This disparity could induce localized shrinkage and stress release, further facilitating the development of nano-sized pores. Consequently, elevated bismuth ion concentrations enhanced metal coordination crosslinking and modulate gelation rates, resulting in the formation of hierarchical pore structures within the hydrogel.

As illustrated in Fig. 3i, the RHOCF featured multiple dynamic noncovalent metal–ligand interactions, physically entangled polymer networks, and hierarchical architectures at multi-scales. The metal–ligand interactions primarily existed between the bismuth ions and polymer chains (PZS and PVA), effectively replacing the original PZS–PZS and PVA–PVA associations due to the higher binding affinities of Bi–PZS and Bi–PVA coordination (Fig. 3d). Concurrently, stronger intercomponent interactions suppressed polymer chain self-aggregation, reducing phase separation to yield a denser entangled network. This synergistic integration established a robust supramolecular framework that resisted deformation and distributed stress uniformly at the molecular level. On the nano/micro scales, the nanocrystalline domains were transformed into homogeneous, entangled networks and the spatial organization was promoted into multiscale hierarchical structures, ultimately enhancing overall mechanical properties of the material. These physically nonvalent crosslinks were well evidenced by the measurements, DFT calculations, and CG-MD simulations. Upon deformation, the RHOCF exhibited a multistage, adaptive mechanical response. Initially, energy dissipation was dominated by the compression of micro-/nano-scale pores, where applied stress is first dispersed within micron-sized cavities and then transmitted to the nanoscale regions, delaying stress localization and microcrack propagation. With increasing strain, the dynamic metal–ligand bonds underwent sacrificial bond rupture and rapid reformation, while the conformational freedom of entangled chains became increasingly restricted—jointly enhancing network rigidity and initiating a pronounced strain-hardening phase. Concurrently, the lower local polymer chain density and increased configurational freedom in these multiscale pore regions facilitated chain rearrangements, slippage, and partial unfolding. This dynamic adaptability enabled efficient energy dissipation and reduces the likelihood of main-chain scission, thereby improving overall toughness. Notably, weak coordination bonds acted as sacrificial units, readily breaking to dissipate mechanical energy and mitigating stress concentration, whereas strong coordination bonds served as structural anchors, maintaining the network's mechanical integrity and ensuring high strength and modulus. The synergistic effect between these dynamic interactions forms a multiscale, self-adaptive energy dissipation mechanism, analogous to natural load-bearing tissues (Supplementary Fig. 14). Such integration of consolidated supramolecular networks and multiscale hierarchical architectures enabled the RHOCF to achieve simultaneous enhancements in toughness, stretchability, and fatigue resistance, with its excellent mechanical performance fundamentally rooted in this synergistic design (Fig. 3i).

Integrated properties of the RHOCF

The synergistic integration of the consolidated entangled network and hierarchical porous architecture synergistically contributed to the RHOCF, imparting not only understanding mechanical properties but also a unified set of functions of high transparency, conductivity, anti-freezing, self-adhesive, and multimodal sensing properties. As shown in Fig. 4a, The RHOCF showed great optical transparency, wherein an average transmittance of 96.32% was obtained across the wavelength range of 400–800 nm. This was in sharply contrast to the completely opaque appearance of the control hydrogel, indicating that the introduction of bismuth ions significantly enhanced optical transmittance (Supplementary Fig. 15). This improvement is attributed to the formation of the nanoscale structural uniformity and highly hydrated polymer network, which together minimize light scattering and promote transparency in the visible range. Crucially, following immersion in liquid nitrogen (−196 °C), the RHOCF retained its transparency and structural integrity, whereas the control hydrogel quickly tuned opaque and fractured (Fig. 1e). The freezing-tolerant transparency was attributed to the presence of ample ions bound with water molecules. These features exhibited the promising potential of the RHOCF as optical materials, especially in ultracold scenarios. Concomitantly, the RHOCF could provide favourable electrical and electromechanical properties including high ionic conductivity of up to 5.61 S/m (Supplementary Fig. 16a, b). This is a synergy effect of hierarchically interconnected pores, rich bismuth ions, and ion migration channels provided by the zwitterionic segments of the polymer chain (Fig. 4b and Supplementary Fig. 16b)[52]. Importantly, the high conductivity, together with mechanical flexibility and optical transparency of the RHOCF were well maintained even at −30 °C (Supplementary Fig. 17a–c). This is because of its ultralow freezing point (−71.61 °C) caused by the synergistic effect of glycerol and bismuth ions (Fig. 4c and Supplementary Fig. 17d). Specifically, the formation of strong hydration shells and the confinement of water molecules within the porous matrix effectively suppress ice crystallization (Fig. 4d). In addition, the RHOCF was able to form a conformable attachment to human wrist even under joint moving, which offered a cornerstone for wearable electronics (Supplementary Fig. 18a). Surprisingly, it could reversibly and tightly adhere to various objects of both hydrophobic and hydrophilic nonporous surfaces such as steel, poly(ethylene terephthalate) (PET), epoxy resin, poly(dimethyl siloxane) (PDMS), poly(methyl methacrylate) (PMMA), and carbon fiber (Supplementary Fig. 18b). Through lap shear and 90° peeling off experiments, we confirmed the high shear strength of the RHOCF to various substrates, ranging from 5.8 to 21.9 kPa (Fig. 4e). It is worth noting that an appropriate amount of bismuth ions enhanced the adhesive strength of RHOCF due to the formation of metal–ligand coordination interactions between the RHOCF and the substrate (Supplementary Fig. 19)[53]. The strong shear strength could be explained by the diverse chemical bonding within the adhesive interfaces, including metal–ligand coordination, hydrogen bonds, cation–π interactions, dipole–dipole interactions, and electrostatic attractions. The functional comparison between the RHOCF and previous studies is presented in Supplementary Tables 2 and 3, manifesting the advantage of our strategy[54–58].

Potential sensory applications

Given its favorable combination of robust mechanical performance and multifunctionality, the RHOCF was investigated as a sensing material for epidermal electronics. As shown in Fig. 5a, a smart glove was first created using the RHOCF, which integrated multimodal perception capabilities, including thermal, strain, and tactile stimuli. This was facilitated by the optimal combination of high softness, strength, stretchability, and self-adhesion. For example, the smart glove could discern warm or cold objects (Fig. 5b, c and Supplementary Fig. 20), offering potential applications in safeguarding robots in complex thermal environments prior to physical interaction. Different hand gestures could also be recognized with the glove, indicating its tremendous potential in wearable epidermal devices (Fig. 5d). This stemmed from the good strain–sensing capabilities of RHOCF, which

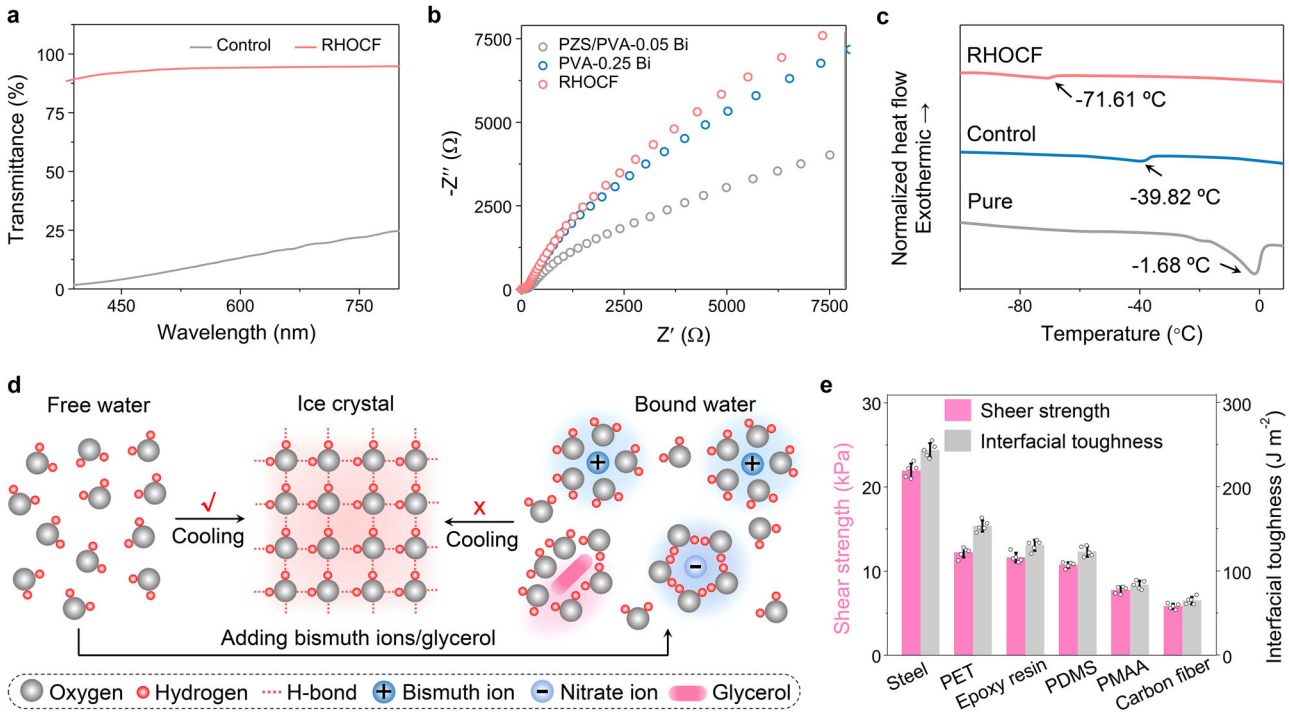

Fig. 4 | Integrated properties of the RHOCF. a The optical property of the control and RHOCF samples. Although the control was opaque, the RHOCF exhibited an optical transmittance of 96.32%. **b** The Nyquist plot of as-prepared samples demonstrated that the enhanced conductivity of RHOCF arisen from the synergistic interaction between bismuth ions and the zwitterionic channels. **c** DSC tests of pure hydrogel, hydrogel containing glycerol (Control sample), and hydrogel containing glycerol/bismuth ions (RHOCF sample). **d** The schematic illustration of molecular interaction between ions/glycerol and water molecules, indicating the anti-freezing mechanism. **e** Shear strength and interfacial toughness of the RHOCF to various substrates. The circular dots of the histogram represented the measured data points of five. Data are presented as mean ± standard deviation from $n = 5$ independent samples.

possessed a sensing range exceeding 1600% and a high sensitivity of approximately 65.31, surpassing most previously reported hydrogel strain sensors (Fig. 5e and Supplementary Fig. 21 and Table 4). Interestingly, monitoring capacitance changes in the RHOCF upon contact with a surface enabled the detection of sensing signals, facilitating the recognition of touches including static and dynamic (Fig. 5f, g and Supplementary Fig. 22). It has been demonstrated that static and dynamic touch patterns could be exploited for remote-controlled human–machine communications via Morse code (Fig. 5h).

The RHOCF also could highly effectively record weaker bioelectrical signals, which typically have amplitudes in the microvolt range. These signals are fundamental physiological indicators closely related to the body's health status. As a proof of concept, electroencephalogram (EEG) recording was chosen because it presents greater challenges compared to electrocardiography (ECG) and electromyography (EMG)[59]. The RHOCF demonstrated high-fidelity EEG recording, showing no significant differences including signal amplitude, shape, and power spectral density in the same period of acquisition compared to signals recorded by the commercial EEG electrode (Supplementary Fig. 23a). The RHOCF exhibited an enhanced resistance capacity to motion as well, which have been proved by daily actions such as blinking, teeth clenching, and turning head (Supplementary Fig. 23b). Additionally, a rigorous EEG-based six-level sustained attention evaluation system was designed to further assess the RHOCF in EEG recording (Fig. 5i and Supplementary Figs. 24 and 25). The RHOCF showed a high accuracy of 90.2% in identifying six levels of sustained attention, compared to 66.5% achieved by the commercial gel electrode (Supplementary Fig. 25)[60]. Figure 5i illustrated a LED with six colors connected to the field programmable gate array, providing real-time feedback on the sustained attention level. During the test, the estimated level of the sustained attention gradually increased from one to six (Supplementary Movie 1).

Discussion

In summary, we demonstrated a tough zwitterionic hydrogel via a consolidated supramolecular network and a spatially hierarchical structure. This approach endowed the RHOCF with mechanically robust performance and good combination of functional merits. The orchestrated integration of functions similar to strong/tough biological tissues is challenging to fulfill in its artificial analogs, including super stretchable (1635% strain), strongly tensile (7.93 MPa), great mechanically rigid (76.85 MJ m^{-3}), great resilient (95.65%), good viscoelastic, sufficiently self-adhesive, as well as advanced multimodal perception. Note that bismuth ions in the RHOCF matrix not only realized the construction of a desirable consolidated supramolecular networks and a hierarchical structure across multiple length scales, leading to high transparency (96.32%) and high conductivity (5.61 S m^{-1}) but also synergized with glycerol, enabling the hydrogel to obtain brilliant freezing tolerance (−71.61 °C). Intriguingly, multiple sensing properties (e.g., strain, thermal, touch, and electrophysiological signal) were simultaneously achieved for the RHOCF. In view of the optimized combination of optical transparency, adhesive capacity, and ambient stability, the RHOCF demonstrates tremendous potential as a highly sensitive and durable sensor to be applied in epidermal electronics, human–machine interfaces, intelligent robots, etc. We anticipate that the proposed concept may offer a potential versatile platform and tool readily extended to prepare other soft conductive materials with a set of function combinations.

Methods

Materials

[2-(Methacryloyloxy) ethyl] dimethyl-(3-sulfopropyl) ammonium hydroxide (EDMAH), bismuth nitrate pentahydrate ($Bi(NO_3)_3{\cdot}5H_2O$) and glycerol were purchased from Aladdin Biochemical Co. Acrylic acid (AA) and polyvinyl alcohol (PVA) was bought from Tianjin Damao

https://doi.org/10.1038/s41467-025-64498-5

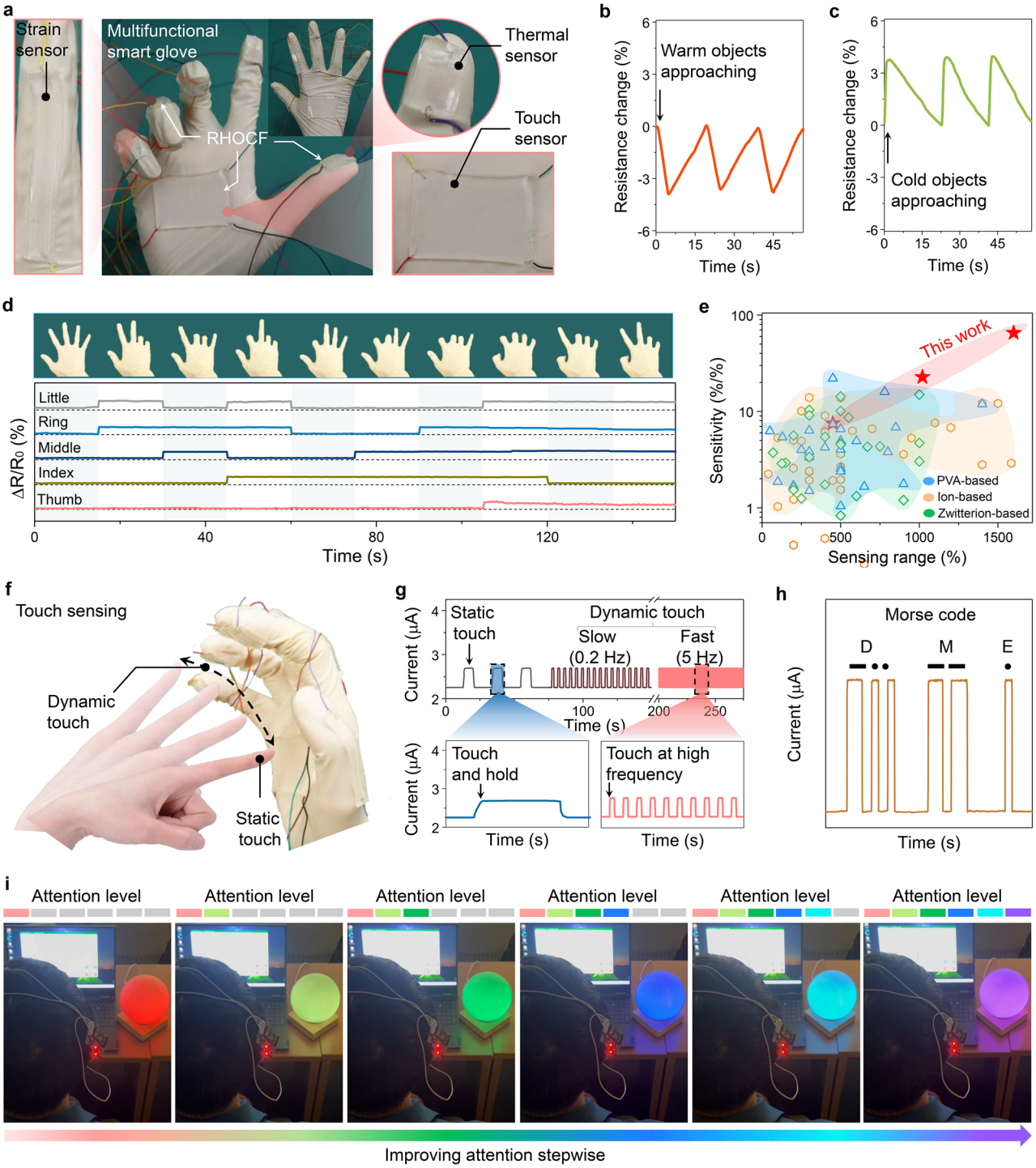

Fig. 5 | Demonstration of RHOCF-based smart soft electronics. a Demonstration of a smart glove that integrates thermal (at fingertips), strain (at fingers), and touch (at palm and back of hand) sensing capacities using the RHOCF. Signals from the glove upon approaching warm (**b**) and cold (**c**) items. **d** Multichannel monitoring of gestures with five adhered RHOCF strain sensors. **e** Working range and sensitivity of this work compared with the reported literature in recent years. **f** Diagram illustrating the haptic sensing capability of the glove in response to finger touches. **g** Signals were produced using the glove via different tactile behaviors such as static (touch and hold) and dynamic (low-/high-frequency). **h** Translated tactile behaviors into Morse code for applications in human–machine interfaces. **i** The demonstration of the proposed sustained attention evaluation system.

Chemical Reagent Co. and Macklin Biochemical Co., respectively. Europium nitrate pentahydrate ($Eu(NO_3)_3{\cdot}5H_2O$), aluminum chloride hexahydrate ($AlCl_3{\cdot}5H_2O$), cobalt chloride hexahydrate ($CoCl_2{\cdot}5H_2O$), calcium chloride ($CaCl_2$), zinc chloride ($ZnCl_2$), Iron chloride ($FeCl_3$), and initiator ammonium persulphate (APS) was provided from Sigma-Aldrich Co. Poly(dimethylsiloxane) (PDMS) film was supplied by Hangzhou Bald Advanced Materials Co. All chemical reagents are used as supplied without any purification. Ultrapure water (18.2 MΩ; Millipore Co., USA) was used in all experiments.

Preparation of the RHOCF

The RHOCF was synthesized via a facile procedure as follows: First, EDMAH and AA were added into the glycerol aqueous solution (1:2 mass radio of water to glycerol) and stirred for 30 min to form uniform

solution (namely, polyzwitterionic salt (PZS), Mixture A). Then, the initiator APS (0.06 g) was added to above solutions and stirred for another 15 min. At the same time, PVA powders with different amounts were slowly added to the glycerol aqueous solution under strong stirring at a temperature of 90 °C until a homogeneous solution formed. After PVA solutions were cooled to room temperature, varied $Bi(NO_3)_3{\cdot}5H_2O$ weights were added to the above under vigorous stirring for 0.5 h until the particles were completely dissolved (Mixture B). The weight percentage of $Bi(NO_3)_3{\cdot}5H_2O$ was changed from 0 to 35 wt.%, with respect to the sum weight of the EDMAH and AA monomers, thus the weight ratio, σ, of $Bi(NO_3)_3{\cdot}5H_2O$:EDMAH/AA was adjusted from 0.05 to 0.35, and the control simple was the PZS/PVA hydrogel (σ=0). Subsequently, the mixture A was added into the mixture B with stirring for another 25 min to obtain the RHOCF blend solution. After 1 hour of sonication for degassing, a clear solution was achieved. It should be noted that all hydrogel fabrication processes were conducted inside a glove box filled with nitrogen. To obtain RHOCF films, the above solution was blown with argon in an argon atmosphere to remove dissolved oxygen. Lastly, the final mixtures were cast in a polymethylmethacrylate (PMMA) mold and cured under ultraviolet light (365 nm, 35 W) for 0.5 h, afterwards, the mold was frozen and thrown repeatedly to obtain the RHOCF.

ATR-FTIR and XPS characterizations

The binding information of characteristic groups was studied using Fourier transform infrared spectrometer (Nicolet IS50 spectrometer, Thermo fisher Scientific Co. USA) equipped with attenuated total reflection (ATR) accessory, and X-ray photoelectron spectroscopy (XPS, Escalab 250Xi, Thermo Fisher Scientific Co. USA). It should be noted that the hydrogel samples should be freeze-dried before testing.

X-ray scattering characterizations

The wide-angle X-ray scattering (WAXS) and the small-angle X-ray scattering (SAXS) measurements were conducted on the beamline BL16B1 (Shanghai Synchrotron Radiation Facility). The wavelength is $\lambda = 1.24$ Å, and a MAR CCD detector is employed. An exposure time of 40 s was used for the both measurements, with a sample-to-detector distance of 2036.4 mm.

SEM characterizations

Hydrogels were made for observing the surface morphologies via a Zeiss Supra 55 filed-emission scanning electron microscope (SEM, Carl Zeiss AG, Germany). The films were soaked in fresh deionized water for 48 h, then the water on the surface was removed. The hydrogel samples were then frozen using liquid nitrogen, and lyophilized in a freeze drier. Before SEM measurements, sample surfaces were coated with gold.

Transmittance characterizations

The optical transmittance of hydrogel samples was measured by a Lambda-950 UV-vis spectrometer (PerkinElmer Co. USA) in a wavelength range of 400–800 nm.

DSC characterizations

Differential scanning calorimetry (DSC, DSC 4000, PerkinElmer Co. USA) was employed to quantify the freezing resistance of hydrogels. The sample was equilibrated at −150 °C for 30 min and heated to 15 °C (2 °C/min). The sample loading was about 25 mg, and the reference was the empty pan.

Tensile tests

Tensile tests were carried out via a WDW3100 mechanical tester. Samples with dimensions of 20 mm length, 15 mm width, and 2 mm thickness were used to evaluate their tensile behaviors at a stretching rate of 50 mm min^{-1}.

Fatigue tests

The single-edge notch method was employed to determine the fatigue threshold of the RHOCF. The sample with dimensions of a width of 6 mm, thickness of 0.2 mm, and gauge length of 10 mm were used. Notched specimens with initial crack length (approximately 1/5 of the width of the sample) were cyclically stretching at a strain rate of 3 % s^{-1} without any pause. The energy release rate (ξ) of the notched sample during the Nth cycle was calculated using the following equation:

$$\xi(N) = 2c(N) \cdot L(N) \cdot Q(N)$$

Where $c(N)$ represents a function of strain variation, defined as $c(N) = 3/\sqrt{\alpha+1}$, $L(N)$ denotes the crack propagation length, and $Q(N)$ refers to the strain energy density of unnotched samples of the same dimensions stretched to the same strain α. The strain energy density $Q(N)$ of unnotched specimens during the Nth cycle can be obtained using $Q(N) = \int_0^{\alpha} \sigma d\alpha$.

Electrical tests

A sample with dimensions of 20 mm length, 10 mm width, and 2 mm thickness was employed for electrical characterizations. A standard four-point probe (Model 34461 A Keysight) would be used to measure the conductivity. The conductivity of the sample could be calculated by $\delta = L \times I / W \times T \times V$. Where δ, L, I, W, T, and V are conductivity, length, current, width, thickness, and voltage, respectively.

Adhesion tests

Interfacial toughness was determined by conducting a standard 90° peeling test (ASTM D2861) on adhered samples with a width of 2.5 cm using a mechanical testing machine. All tests were conducted at a consistent peeling speed of 50 mm/min, and the measured force reached a steady state once the peeling process stabilized. The interfacial toughness was able to obtain through dividing the plateau force via the sample's width (for 90° peeling test). Shear strength was determined by conducting a standard lap-shear test (ASTM F2255) on adhered samples with a width of 2.5 cm using a mechanical testing machine. The shear strength could be achieved through dividing the maximum force obtained from the lap-shear test by the adhesive area of the sample.

Density functional theory calculations

Density functional theory (DFT) calculations were conducted on the Gaussian 16 (Revision A.03) computational package and GaussView 6. For metal–ligand coordination interactions, B3LYP functional and the basis set lanl2dz were performed for geometry optimizations, energy calculations and frequency calculations and the D3-version of Grimme's empirical dispersion correction[61]. For hydrogen bond interactions, B3LYP functional[62] and the basis set 6-311 g(d,p)[63] were carried out for geometry optimizations, energy calculations and frequency calculations via counterpoise Basis Set Superposition Error (BSSE) corrections[64] and the D3-version of Grimme's empirical dispersion correction[65]. A conductor-like polarizable continuum solvation model (CPCM) of water and an ultrafine integration grid were applied. All geometries were optimized to a minimum, and frequency calculations were performed at the same level of theory to verify the absence of imaginary frequencies. Multiwfn was used to calculate the electrostatic potential (ESP) distribution of each atom[66,67]. Additionally, VESTA 3 was employed to realize the visualization of optimized structures and composites[68].

Molecular dynamic simulations

The simulations were carried out via commercial software of Materials Studio. The Universal force field was employed to model atomistic interactions among bismuth ions, glycerol molecules, water molecules, and polymer chains[69,70]. A simulation box was constructed

with periodic boundary conditions (PBCs). In control systems, various components including twenty PVA chains, twenty PZS chains, and glycerol molecules were placed in the box, which was subsequently filled with water molecules. In RHOCF systems, 40 bismuth and 120 nitrate ions were also introduced into the simulation box. The initial size of the simulation unit cell is $56.96 \times 56.96 \times 56.96$ Å, with the lattice parameters of $\alpha = \beta = \gamma = 90°$. The models underwent equilibrated at 300 K for 25 ps in the NVT ensemble. Figure 3g ($\alpha = 1$) displayed the equilibrium system of the RHOCF. The loading was applied within the box using an Andersen thermostat to maintain a temperature of 300 K, with no pressure applied in the other two directions. The cutoff value of carbon-carbon single bond was set at 1.80 Å[71,72], implying the potential polymer chain breakage. These calculations were optimized using a smart algorithm method with an energy convergence threshold of 1×10^{-3} kCl/mol and a force convergence threshold of 0.5 kcal/mol per Å.

Sensing demonstrations

A commercial latex glove served as the substrate onto which RHOCF films were integrated. The RHOCF film was connected to copper wire electrodes on each end. As a human hand wearing the smart glove was bent or approached different objects that were warm or cold, changes in resistance as the sensing signals were detected. When used as a touch panel, changes in capacitance were recorded as sensing signals when a human finger touched it. Thereafter, Morse code was implemented to realize human-machine interaction by translating the dynamic touches into signals of different duration, and the short touches corresponded to dots, while the long touches corresponded to dashes. The author affirm that human research participants provided informed consent for publication of the images in Fig. 5.

Electroencephalography signal extraction and multilevel sustained attention evaluation

The EEG signals from forehead were recorded using an epidermal RHOCF electrode. A multichannel signal analysis system was constructed and connected to the RHOCF, facilitated by Bluetooth module to realize their wireless transmission. The raw EEG signals could be extracted using custom Discrete Fourier Transform (DFT), and Pearson correlation analysis was used to determine the features. Subsequently, a machine-learning based classifier was employed to output the real-time sustained attention level, which was indicated via the color of LED light. The assessment of EEG signals adhered to all ethical guidelines under protocol NUS-IRB-2023-922, which received approval from the Institutional Review Board of the National University of Singapore.

Reporting summary

Further information on research design is available in the Nature Portfolio Reporting Summary linked to this article.

Data availability

The data that support the findings of this study are available from the corresponding authors upon request. Source data are provided with this paper.

References

1. Zhang, E. et al. An injectable and biodegradable zwitterionic gel for extending the longevity and performance of insulin infusion catheters. *Nat. Biomed. Eng.* **8**, 1197–1213 (2024).
2. Nasseri, R. et al. Programmable nanocomposites of cellulose nanocrystals and zwitterionic hydrogels for soft robotics. *Nat. Commun.* **14**, 6108 (2023).
3. Guo, X. et al. Anti-freezing self-adhesive self-healing degradable touch panel with ultra-stretchable performance based on transparent triboelectric nanogenerators. *Adv. Func. Mater.* **32**, 2201230 (2022).
4. Jiang, Z. et al. Anti-swelling zwitterionic nanocomposite hydrogels with biocompatibility as flexible sensor for underwater application. *Eng. Sci.* **31**, 1200 (2024).
5. Yao, M. et al. Microgel reinforced zwitterionic hydrogel coating for blood-contacting biomedical devices. *Nat. Commun.* **13**, 5339 (2022).
6. Li, X. et al. Pure zwitterionic hydrogel with mechanical robustness and dynamic tunability enabled by synergistic non-covalent interactions. *Adv. Func. Mater.* **34**, 2409594 (2024).
7. Ren, J. et al. Super-tough, non-swelling zwitterionic hydrogel sensor based on the Hofmeister effect for potential motion monitoring of marine animals. *Adv. Mater.* **36**, e2412162 (2024).
8. Huang, K. T. et al. Zwitterionic gradient double-network hydrogel membranes with superior biofouling resistance for sustainable osmotic energy harvesting. *Adv. Func. Mater.* **33**, 2211316 (2023).
9. Gong, J. P. Why are double network hydrogels so tough? *Soft Matter* **6**, 2583–2590 (2010).
10. Zhao, X. Multi-scale multi-mechanism design of tough hydrogels: building dissipation into stretchy networks. *Soft Matter* **10**, 672–687 (2014).
11. Tang, L. et al. Multifunctional nanocellulose hydrogels featuring superior injectability, self-healing, adhesion, and near-infrared photothermal antibacterial activity. *ES Mater. Manuf.* **28**, 1522 (2025).
12. Ritchie, R. O. The conflicts between strength and toughness. *Nat. Mater.* **10**, 817–822 (2011).
13. Li, Q. et al. Zwitterionic biomaterials. *Chem. Rev.* **122**, 17073–17154 (2022).
14. Wang, Z. et al. Recent advances in zwitterionic hydrogels: structure, applications and challenges. *J. Mater. Chem. A* **13**, 13693–13705 (2025).
15. Ding, Y. et al. Humidity-resistant wearable triboelectric nanogenerator utilizing a bound-water-rich zwitterionic hydrogel with microphase-separated domains. *Adv. Func. Mater.* **35**, 2421164 (2024).
16. Xu, X. et al. Bioinspired double network hydrogels: from covalent double network hydrogels via hybrid double network hydrogels to physical double network hydrogels. *Mater. Horiz.* **8**, 1173–1188 (2021).
17. Guo, X. et al. A skin- mimicking multifunctional hydrogel via hierarchical, reversible noncovalent interactions. *Sci. Adv.* **11**, eadv8523 (2025).
18. Wang, G. et al. Supramolecular zwitterionic hydrogels for information encryption, soft electronics and energy storage at icy temperature. *Adv. Func. Mater.* **35**, 2505048 (2025).
19. Zhang, Y. S. et al. Advances in engineering hydrogels. *Science* **356**, eaaf3627 (2017).
20. Li, X. et al. Design principles for strong and tough hydrogels. *Nat. Rev. Mater.* **9**, 380–398 (2024).
21. Zhao, X. et al. Soft materials by design: unconventional polymer networks give extreme properties. *Chem. Rev.* **121**, 4309–4372 (2021).
22. Zhang, W. et al. Kinetics-boosted effect enabled by zwitterionic hydrogel electrolyte for highly reversible zinc anode in zinc-ion hybrid micro-supercapacitors. *Adv. Energy Mater.* **12**, 2202219 (2022).
23. Guo, W. Y. et al. Multifunctional MXene conductive zwitterionic hydrogel for flexible wearable sensors and arrays. *ACS Appl. Mater. Interfaces* **15**, 24933–24947 (2023).
24. Wang, Y. et al. Ultrarobust, tough and highly stretchable self-healing materials based on cartilage-inspired noncovalent assembly nanostructure. *Nat. Commun.* **12**, 1291 (2021).
25. Fu, L. et al. Cartilage-like protein hydrogels engineered via entanglement. *Nature* **618**, 740–747 (2023).

26. Huang, J. et al. One-pot construction of articular cartilage-like hydrogel coating for durable aqueous lubrication. *Adv. Mater.* **36**, e2309141 (2024).
27. Lin, S. et al. Muscle-like fatigue-resistant hydrogels by mechanical training. *Proc. Natl. Acad. Sci. USA* **116**, 10244–10249 (2019).
28. Kim, I. H. et al. Human-muscle-inspired single fibre actuator with reversible percolation. *Nat. Nanotechnol.* **17**, 1198–1205 (2022).
29. Chen, Q. et al. Bilayer hydrogels with low friction and high load-bearing capacity by mimicking the oriented hierarchical structure of cartilage. *ACS Appl. Mater. Interfaces* **14**, 52347–52358 (2022).
30. Park, H. et al. Toughening self-healing elastomer crosslinked by metal-ligand coordination through mixed counter anion dynamics. *Nat. Commun.* **14**, 5026 (2023).
31. Hua, M. et al. Strong tough hydrogels via the synergy of freeze-casting and salting out. *Nature* **590**, 594–599 (2021).
32. Nepal, D. et al. Hierarchically structured bioinspired nanocomposites. *Nat. Mater.* **22**, 18–35 (2023).
33. El-Sewify, I. M. et al. Dual colorimetric and fluorometric monitoring of Bi^{3+} ions in water using supermicroporous Zr-MOFs chemosensors. *J. Lumin.* **198**, 438–448 (2018).
34. Griffith, D. M. et al. Medicinal chemistry and biomedical applications of bismuth-based compounds and nanoparticles. *Chem. Soc. Rev.* **50**, 12037–12069 (2021).
35. Xiang, X. et al. Flower-like bismuth metal-organic frameworks grown on carbon paper as a free-standing electrode for efficient electrochemical sensing of Cd^{2+} and Pb^{2+} in water. *Eng. Sci.* **3**, 77–83 (2018).
36. Sun, H. et al. Bismuth in medicine. *Met. Ions Biol. Syst.* **41**, 333–378 (2004).
37. Yang, N. et al. Biocoordination chemistry of bismuth: recent advances. *Coord. Chem. Rev.* **251**, 2354–2366 (2007).
38. Zhao, Y. et al. A self-healing electrically conductive organogel composite. *Nat. Electron.* **6**, 206–215 (2023).
39. Zhang, Y. et al. Peptide-enhanced tough, resilient and adhesive eutectogels for highly reliable strain/pressure sensing under extreme conditions. *Nat. Commun.* **13**, 6671 (2022).
40. Xiong, X. et al. Polymerizable rotaxane hydrogels for three-dimensional printing fabrication of wearable sensors. *Nat. Commun.* **14**, 1331 (2023).
41. Liu, X. et al. A microphase-separated design toward an all-round ionic hydrogel with discriminable and anti-disturbance multisensory functions. *Adv. Mater.* **36**, e2309508 (2024).
42. Zhang, L. et al. Cellulose nanofiber-mediated manifold dynamic synergy enabling adhesive and photo-detachable hydrogel for self-powered E-skin. *Nat. Commun.* **15**, 3859 (2024).
43. Xu, L. et al. A solvent-exchange strategy to regulate noncovalent interactions for strong and antiswelling hydrogels. *Adv. Mater.* **32**, e2004579 (2020).
44. Mousa, M. et al. Elastic behavior of nanophases in polyvinyl alcohol (PVA)/bamboo charcoal (BC) nanocomposite films. *Front. Mater.* **5**, 44 (2018).
45. Agger, J. R. et al. Crystallization in zeolite A studied by atomic force microscopy. *J. Am. Chem. Soc.* **120**, 10754–10759 (1998).
46. McLean, R. S. et al. High-resolution imaging of ionic domains and crystal morphology in ionomers using AFM techniques. *Macromolecules* **33**, 6541–6550 (2000).
47. Land, T. A. et al. Mechanisms of protein crystal growth: an atomic force microscopy study of canavalin crystallization. *Phys. Rev. Lett.* **75**, 2774–2777 (1995).
48. Pan, L. et al. Hierarchical nanostructured conducting polymer hydrogel with high electrochemical activity. *Proc. Natl. Acad. Sci. USA* **109**, 9287–9292 (2012).
49. Cai, G. et al. Metal-organic framework-based hierarchically porous materials: synthesis and applications. *Chem. Rev.* **121**, 12278–12326 (2021).
50. Wychowaniec, J. K. et al. Hierarchical porous metal-organic gels and derived materials: from fundamentals to potential applications. *Chem. Soc. Rev.* **51**, 9068–9126 (2022).
51. Yang, X. Y. et al. Hierarchically porous materials: synthesis strategies and structure design. *Chem. Soc. Rev.* **46**, 481–558 (2017).
52. Xu, S. et al. Force-induced ion generation in zwitterionic hydrogels for a sensitive silent-speech sensor. *Nat. Commun.* **14**, 219 (2023).
53. Ma, X. et al. Hydrogels for underwater adhesion: adhesion mechanism, design strategies and applications. *J. Mater. Chem. A* **10**, 11823–11853 (2022).
54. Shi, J. et al. Active biointegrated living electronics for managing inflammation. *Science* **384**, 1023–1030 (2024).
55. Chen, L. et al. A hyperelastic hydrogel with an ultralarge reversible biaxial strain. *Science* **383**, 1455–1461 (2024).
56. Zhang, Y. et al. A microscale soft ionic power source modulates neuronal network activity. *Nature* **620**, 1001–1006 (2023).
57. Bao, B. et al. Rapid fabrication of physically robust hydrogels. *Nat. Mater.* **22**, 1253–1260 (2023).
58. Ohm, Y. et al. An electrically conductive silver-polyacrylamide-alginate hydrogel composite for soft electronics. *Nat. Electron.* **4**, 185–192 (2021).
59. Tian, Q. et al. Hairy-skin-adaptive viscoelastic dry electrodes for long-term electrophysiological monitoring. *Adv. Mater.* **35**, e2211236 (2023).
60. Han, Q. et al. Hydrogel nanoarchitectonics of a flexible and self-adhesive electrode for long-term wireless electroencephalogram recording and high-accuracy sustained attention evaluation. *Adv. Mater.* **35**, e2209606 (2023).
61. Wadt, W. R. et al. Ab initio effective core potentials for molecular calculations. Potentials for main group elements Na to Bi. *J. Chem. Phys.* **82**, 284–298 (1985).
62. Becke, A. D. Density-functional thermochemistry. I. The effect of the exchange-only gradient correction. *J. Chem. Phys.* **96**, 2155–2160 (1992).
63. Krishnan, R. et al. Self-consistent molecular orbital methods. XX. A basis set for correlated wave functions. *J. Chem. Phys.* **72**, 650–654 (1980).
64. Simon, S. et al. How does basis set superposition error change the potential surfaces for hydrogen-bonded dimers? *J. Chem. Phys.* **105**, 11024–11031 (1996).
65. Elstner, M. et al. Hydrogen bonding and stacking interactions of nucleic acid base pairs: a density-functional-theory based treatment. *J. Chem. Phys.* **114**, 5149–5155 (2001).
66. Lu, T. et al. Multiwfn: a multifunctional wavefunction analyzer. *J. Comput. Chem.* **33**, 580–592 (2012).
67. Zhang, J. et al. Efficient evaluation of electrostatic potential with computerized optimized code. *Phys. Chem. Chem. Phys.* **23**, 20323–20328 (2021).
68. Momma, K. et al. VESTA3 for three-dimensional visualization of crystal, volumetric and morphology data. *J. Appl. Crystallogr.* **44**, 1272–1276 (2011).
69. Wang, Y. et al. Compliant and robust tissue-like hydrogels via ferric ion-induced of hierarchical structure. *Adv. Func. Mater.* **33**, 2210224 (2023).
70. Wang, N. et al. Ultrarobust subzero healable materials enabled by polyphenol nano-assemblies. *Nat. Commun.* **14**, 814 (2023).
71. Guo, X. et al. Strong and tough fibrous hydrogels reinforced by multiscale hierarchical structures with multimechanisms. *Sci. Adv.* **9**, eadf7075 (2023).
72. Tolladay, M. et al. Interatomic forces breaking carbon-carbon bonds. *Carbon* **175**, 420–428 (2021).

Acknowledgements

This work is supported by A*STAR under its IAF PP Grant (Project No. M22K5a0045).

Author contributions

W.Z. and X.G. conceived the idea and designed the experiments. W.Z. supervised the project. X.G., C.C., H.Y., T.L. and H.Q. conducted the experiments and contributed to the data analysis. L.Z. and H.Z. performed the CG-MD and DFT simulations. X.G. and W.Z. wrote and revised the manuscript. All authors discussed the research and reviewed the manuscript before submission.

Competing interests

The authors declare no competing interests.

Additional information

Supplementary information The online version contains supplementary material available at https://doi.org/10.1038/s41467-025-64498-5.

Correspondence and requests for materials should be addressed to Wei Zhai.

Peer review information *Nature Communications* thanks Shaoxing Qu and the other, anonymous, reviewers for their contribution to the peer review of this work. A peer review file is available.

Reprints and permissions information is available at http://www.nature.com/reprints

Publisher's note Springer Nature remains neutral with regard to jurisdictional claims in published maps and institutional affiliations.

Open Access This article is licensed under a Creative Commons Attribution-NonCommercial-NoDerivatives 4.0 International License, which permits any non-commercial use, sharing, distribution and reproduction in any medium or format, as long as you give appropriate credit to the original author(s) and the source, provide a link to the Creative Commons licence, and indicate if you modified the licensed material. You do not have permission under this licence to share adapted material derived from this article or parts of it. The images or other third party material in this article are included in the article's Creative Commons licence, unless indicated otherwise in a credit line to the material. If material is not included in the article's Creative Commons licence and your intended use is not permitted by statutory regulation or exceeds the permitted use, you will need to obtain permission directly from the copyright holder. To view a copy of this licence, visit http://creativecommons.org/licenses/by-nc-nd/4.0/.

© The Author(s) 2025